THE PERMIAN VOLCANICS OF CENTRAL ALBORZ: IMPLICATIONS FOR PASSIVE CONTINENTAL MARGIN ALONG THE SOUTHERN BORDER OF PALEOTETHYS

Morteza Delavari*,✉, Asghar Dolati*, Ali Mohammadi** and **Farzaneh Rostami***

* *Faculty of Earth Sciences, Kharazmi University, Tehran, Iran.*
** *Department of Earth Sciences, ETH Zurich, Switzerland.*
✉ *Corresponding author, email: delavarimza@gmail.com; delavari@khu.ac.ir*

Keywords: *Alkaline basalt, intra-plate volcanism, Permian, Central Alborz.*

ABSTRACT

The Permian volcanics of Central Alborz (PVCA) crop out between the Ruteh and Nesen Formations in the Baladeh-Siahbisheh area. The volcanics are predominantly basaltic and plagioclase-phyric. Ferromagnesian minerals such as clinopyroxene and olivine are not modally abundant and sometimes are totally altered. Chemical composition of clinopyroxene is characterized by high TiO_2 contents (4.9-7.2 wt.%). Based on whole rock geochemistry, the samples display sodic alkaline nature (Na_2O = 3.7 to 7.8 wt.%). Chondrite-normalized rare earth element (REE) patterns are extremely LREE-enriched with $(La/Yb)_N$ of 8.3-20.5. Both normalized REE and multi-element diagrams represent ocean island basalt (OIB) characteristics. Modeling based on trace element values, and the content of some major elements reveal low partial melting degree (< 10%) of a deep garnet-bearing mantle source. As the samples geochemically show an intra-plate tectonomagmatic setting without subduction zone signatures, during the Permian (and earlier times), the Alborz area was possibly a passive continental margin along the southern border of Paleotethys. As a result, the Alborz Permian magmatism could have been reasonably induced by an extensional tectonic regime along the northward-moving Cimmerian terranes during the early stages of Neotethys development.

INTRODUCTION

Iran is a collage of Cimmerian microplates including Alborz, Sanandaj-Sirjan and central Iran. They became detached from the northern margin of Gondwana during the opening of Neotethys in Permian time, and got accreted to Laurasia in mid to Late Triassic as a result of the closure of Paleotethys (Stampfli, 2000; Stampfli et al., 2002; Golonka, 2004; 2007; Gaetani et al., 2009; Wilmsen et al., 2009; Zanchi et al., 2009; Zanchetta et al., 2013). The Alborz range in northern Iran extends with a gentle curved shape, from Azerbaijan and the Lesser Caucasus to the west to northern Afghanistan to the east (Fig. 1a). On the basis of lithofacies analyses, Alavi (1996) characterized seven tectonostratigraphic units in the Alborz system from Precambrian to Cenozoic; the older ones are made of late Precambrian to Early Ordovician epicontinental platform sequences, Middle Ordovician to Devonian magmatic rocks and Devonian to Middle Triassic continental shelf sequences. The Paleozoic magmatic rocks of Iran are not abundant with respect to those of Mesozoic and Cenozoic age; however, their multiple phases of formation during Ordovician-Silurian, Devonian-Carboniferous and Permian times (Berberian and King, 1981) suggest important tectonic events related to the formation of the Paleotethyan and Neotethyan oceans.

In this scenario, the study of Permian magmatic rocks of Central Alborz could be useful to better understand its tectonic setting during late Paleozoic. The study area in Central Alborz includes a volcanic unit occurring as an interlayer in the Middle to Late Permian formations.

This is the first geochemical study of these rocks. In this paper, we present new petrographical and geochemical data on both mineral and whole rocks, to shed light on their petrogenesis, including melt source characteristics and tectonic environment of melt formation.

GEOLOGICAL SETTING

The study area is part of Central Alborz, located to the northeast of the town of Baladeh, between 51°10´ to 51°56´ East longitude and 36°13´ to 36°22´ North latitude (Fig. 1b, c). A lot of sedimentary formations of Precambrian-Cambrian (Kahar and Soltanieh Formations), Carboniferous (Mobarak Formation), Triassic-Jurassic (Elika Formation and Shemshak Group), Cretaceous (Tizkuh Formation) and Eocene age (Karaj Formation) are largely exposed in this area (Amol 1:250,000 geological map; Vahdati Daneshmand, 1991).

In the stratigraphic sequence, the Mobarak Formation (Carboniferous), due to a sedimentary hiatus lies unconformably onto the Cambrian units. Furthermore, due to the long-lasting tectonic activity of the Alborz domain especially during the Cimmerian and Alpine orogenic cycles, many contacts are faulted. Overall, the tectonics of the Alborz system is dominantly controlled by thrust faults (Fig. 1b).

In the study area, the faults which controlled the tectonic movements and deformational structures are thrusts with nearly east-west trends. The faults dip both north and southwards, although the latter ones are more common (Vahdati Daneshmand, 1991). Despite these tectonic displacements, the late Paleozoic units display lithostratigraphic sequences with well-preserved primary contacts. During the Permian, two gaps in sedimentation occurred between the Dorud-Ruteh and Ruteh-Nesen Formations (Gaetani et al., 2009). Also, during this time, two different volcanic units are reported in Central Alborz: one at the base of the Nesen Formation and the other within the upper part of the Ruteh Formation (Gaetani et al., 2009). The studied volcanic unit is located just below the Nesen Formation, without any gap (Fig. 2). It is approximately 30 to 50 m thick, more than 20 km long, from the Siahbisheh to Baladeh towns, and can be observed in the northeast of Baladeh (Fig. 1c).

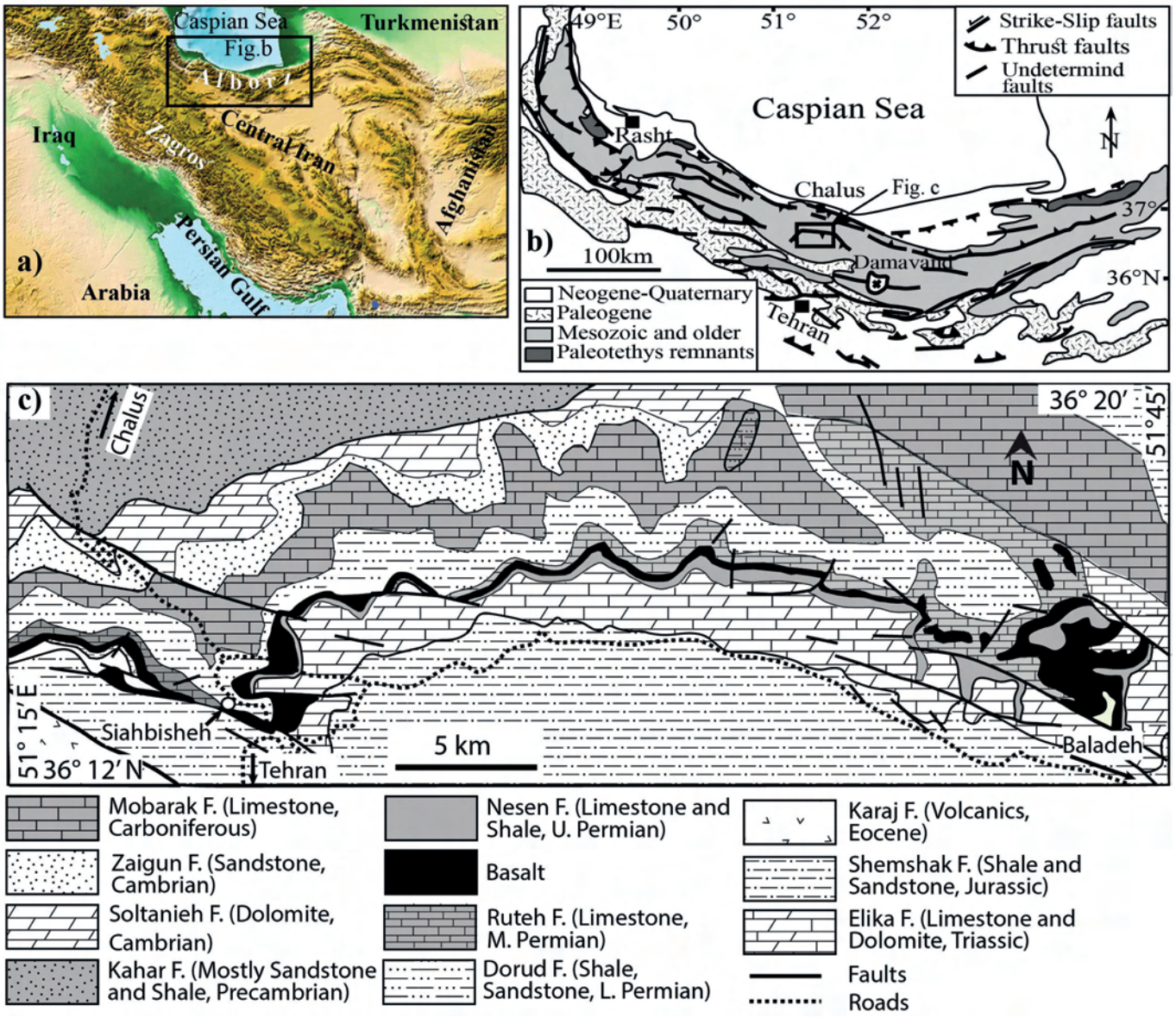

Fig. 1 - (a) Location of the Alborz Mountain belt in Iran within the frame of the Arabia-Eurasia collision. (b) Simplified geologic map of Alborz, modified from Allen et al. (2003). (c) Simplified geologic map of the study area (modified from Vahdati Daneshmand, 1991).

ANALYTICAL METHODS

Crushing and powdering of the samples were performed at the Kharazmi University and Iranian Mineral Processing Research Center (IMPRC), respectively. The analysis of whole-rock samples was conducted by X-ray fluorescence (XRF) and laser ablation-inductively coupled plasma-mass spectrometry (LA-ICP-MS) at the ETH Geological Institute, Zurich. Major and minor element abundances were measured by XRF on fused glass beads using a Panalytical Axios wavelength dispersive spectrometer (WDXRF, 2. 4KV). The homogeneous glass discs were achieved via melting of a mixed lithium tetraborate and rock powder with the ratio of 5:1. The rare earth elements (REEs) and some of other trace elements analyses were carried out by LA-ICP-MS on XRF fused discs calibrated without matrix-matching standards (Günther, 2002). The Spectrometer was set up for 27 trace elements, including REEs and Cs, Rb, Ba, Th, U, Nb, Ta, Ti, Y, Hf, Zr, Pb and Sr. Data-acquisition time per spot was about 1 minute and energy density was 15 J/cm^2 at a frequency of 12 Hz. For each disc, three spots (90 μm diameter) were analysed. As internal standards, concentration of CaO (obtained by XRF analysis) was used and calibrated against NIST 610 for data correction using the SILLS program (Guillong et al., 2008). The expected measuring error is ~ 1%, close to the detection limit, and even smaller at higher concentrations.

Major element compositions of minerals were achieved by electron probe microanalyzer (EPMA), using a superprobe Jeol 8200 machine at the University of California, Los Angeles (UCLA). Operating condition was an acceleration voltage of 15 keV and five spectrometers with a focused beam and counting time of 15-20 s. The most appropriate and updated standards were used for the minerals.

PETROGRAPHY

The samples display porphyritic to seriate textures. They are almost plagioclase-phyric. Major minerals consist of

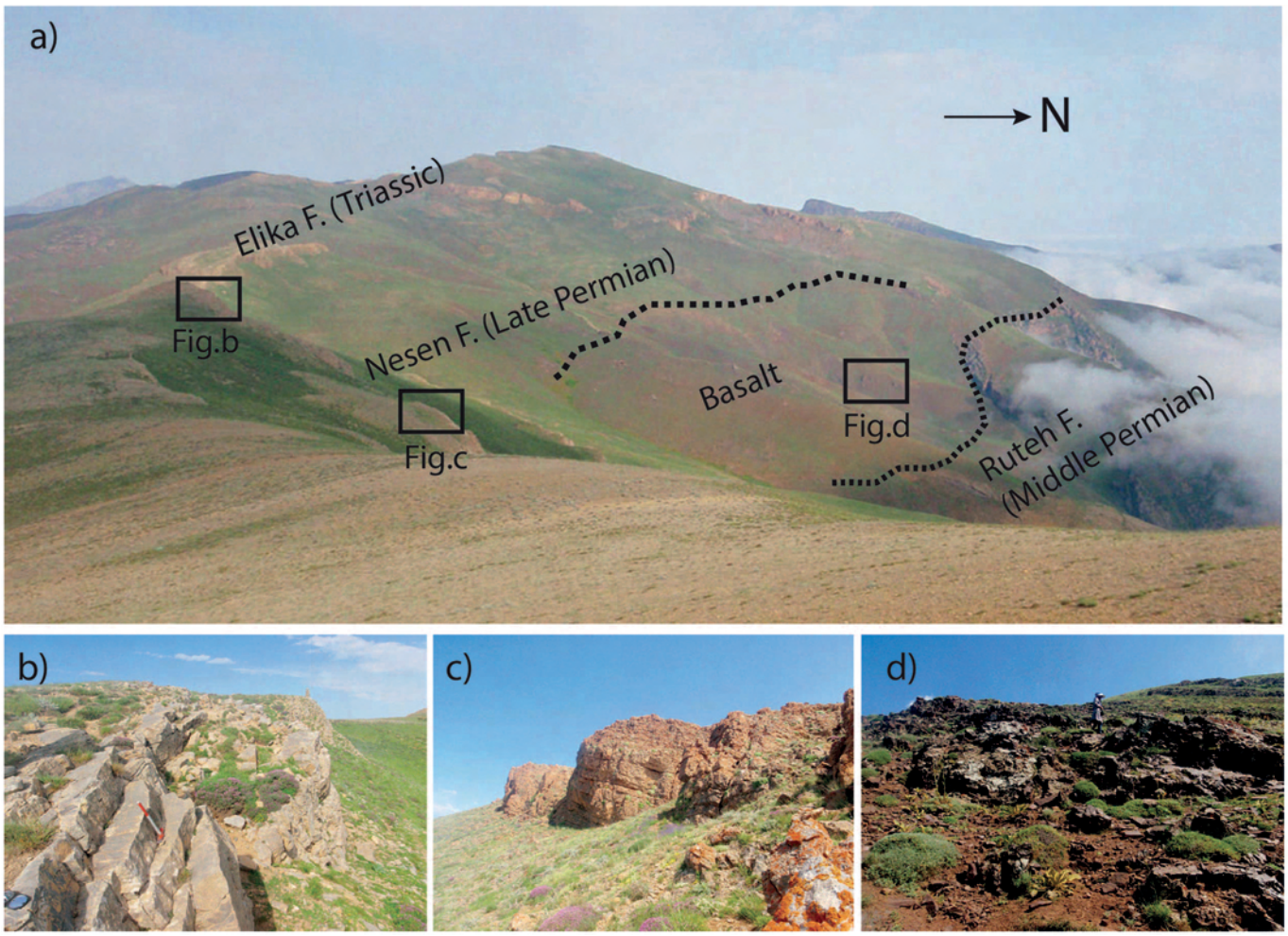

Fig. 2 - (a) Field view of a basaltic unit and its stratigraphic relationships with neighboring sedimentary formations. (b), (c) and (d) outcrop views of the Elika Formation, Nesen Formation and basaltic unit, respectively.

plagioclase, clinopyroxene and olivine. Fe-Ti oxide is the main accessory mineral. Among the phenocrystic phases, plagioclase is the most abundant (Fig. 3a). Furthermore, this mineral commonly appears as microlith in the matrix, forming in some cases more than 50 vol.% of the rock (Fig. 3a to d). Plagioclase phenocrysts are generally subhedral, sometimes up to 5 mm in diameter. The fresh plagioclase crystals usually display polysynthetic twinning. The alteration products of plagioclase include sericite, calcite and, to a lesser extent chlorite.

Fresh ferromagnesian minerals (clinopyroxene and olivine) are not modally abundant. Clinopyroxene is often highly altered, but in some samples fresh crystals can be found (less than 5% of the mode; Fig. 3b). The clinopyroxene phenocrysts are generally less than 1 mm in size. In the matrix, clinopyroxene fills interstitial spaces between plagioclase laths (Fig. 3c). Chlorite is the main alteration product of this mineral. Olivine, although modally scarce, is also observed in a few samples and can be rarely found as fresh phenocrysts. More often, it appears as completely altered, chloritized and uralitized crystals just recognizable by their form and fracture patterns. Opaque minerals (Fe-Ti oxides) generally occur as anhedral fine grains in the matrix (Fig. 3d). They can crystallize directly from the melt or may result from alteration of the ferromagnesian phases. In some samples highly opaque-enriched globular masses with the size of several mm to 1 cm appear, which can be either exsolved parts or the result of secondary processes. From the petrography, the crystallization trend could be stated as olivine, plagioclase, clinopyroxene and Fe-Ti oxides. In these rocks due to long water-rock interaction, some of the vesicles and cracks are filled by calcite.

MINERAL CHEMISTRY

Clinopyroxene

We tried, as far as possible, to analyze the minerals from core to rim but as noted above in some cases, especially in interstitial crystals, the small size does not allow us to do this. In addition, their high alteration makes it difficult to find suitable samples. Representative mineral analyses which were performed on sample MDB-11 are given in Table 1. SiO_2 content ranges from 45.1 to 48.0 wt.%. TiO_2 shows higher content and more variation in the range of 2.6 to 4.1 wt.%. Similarly, Al_2O_3 displays considerable changes from 4.9 to 7.2 wt.%. FeO, MgO and CaO are in the ranges of 6.1 to 7.3, 11.3 to 12.3 and 20.1 to 22.3 wt.%, respectively. Clinopyroxene composition in terms of quadrilateral components is En_{34-36} Fs_{15-18} Wo_{43-47} and plots within the diopside field (Fig. 4b). In one of the crystals analyzed from core to rim, Na_2O, TiO_2 and Al_2O_3 decrease toward the rim but conversely, SiO_2 and MgO represent an increasing trend. For CaO and Mg#, an oscillatory variation is observed.

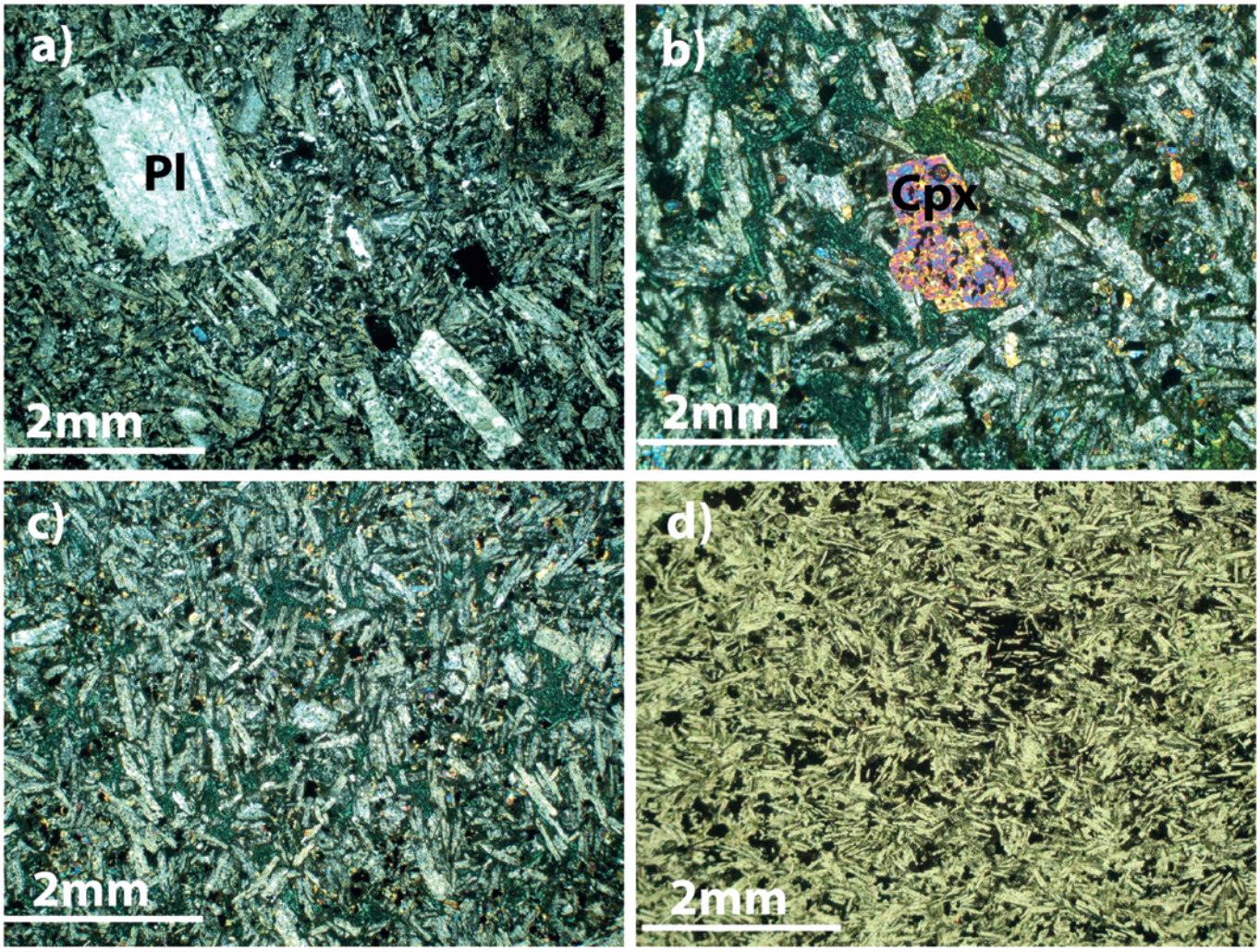

Fig. 3 - Photomicrographs showing the petrographic characteristics of the PVCA. (a) Seriate texture in the volcanic rocks and high modal abundance of plagioclase (Pl) (XPL). (b) Almost fresh subhedral clinopyroxene phenocryst (Cpx) (XPL). (c) Small clinopyroxene crystals with higher interference color filling the interstitial space between plagioclase laths (XPL). (d) Plagioclase laths and interstitial opaque minerals (PPL).

Plagioclase

Representative plagioclase composition is given in Table 2. In the analysed grains, CaO decreases but Na_2O and SiO_2 increase from core to rim. Therefore, plagioclase displays a normal zoning which agrees with crystal growth in a naturally evolving melt. CaO and Na_2O range from 3.6 to 11.1 and 4.6 to 5.8 wt.%, respectively. Furthermore, variations of SiO_2 and Al_2O_3 are 52.9 to 60.7 and 22.9 to 29.1 wt.%, respectively. Overall, plagioclase composition shows limited ranges, almost within the field of labradorite (An% = 49.2-54.9) (Fig. 4a). Except for the altered crystal domains, in all the other points, K_2O does not exceed 0.8 wt.%.

Whole-rock chemistry

The whole-rock chemical analyses are presented in Table 3. LOI value ranges from 1.8 to 6.6 wt.% suggesting high alteration of some samples, which may affect the contents of mobile elements like large ion lithophile elements (LILEs). So, here we used high field strength elements (HFSEs) for the aim of chemical classification. In the Zr/TiO_2 vs. Nb/Y diagram (Winchester and Floyd, 1977; Fig. 5a), all the samples plot within the alkali basalt field. Also, in the total alkali vs. silica diagram (Fig. 5b), the samples have an alkaline signature. On recalculated anhydrous basis, alkali elements indicate high values with Na_2O and K_2O contents of 3.7 to 7.8 and 0.1 to 1.8 wt.%, respectively. Moreover, TiO_2 shows elevated content and varies from 2.4 to 4.1 wt.%. FeO_T is also high in some samples reaching up to 14.2 wt.%, which is consistent with high modal abundances of Fe-Ti oxides. MgO exhibits variation of 1.9 to 5.9 wt.% and Mg# [Mg# = 100* $MgO/(MgO + FeO_T)$] is from 19.7 to 53.4. In selected major and trace elements vs. MgO variation diagrams (Fig. 6), TiO_2 and FeO_T are negatively correlated with MgO at least during the first steps of magma evolution suggesting their concentration in the melt and the lack of Fe-Ti oxide crystallization. Positive correlation between Ni, CaO, CaO/Al_2O_3 and MgO supports fractionation of olivine, clinopyroxene and plagioclase. In the Sr vs. MgO diagram, despite scattered points, a nearly decreasing trend can be observed suggesting, to some extent, plagioclase fractionation. The increasing trend of incompatible trace elements like alkali elements, Ta, Y and Nb with decreasing MgO is compatible with a normal melt evolutionary process. Low Ni (11 to 153 ppm) and Cr (17 to 226 ppm) contents as well as Mg# value (< 53.4) clearly indicate that these rocks do not reflect a primitive melt composition in equilibrium with upper mantle mineralogy and suggest that

they are representative of evolved melts that suffered fractional crystallization of ferromagnesian minerals. The chondrite-normalized rare earth element (REE) patterns are shown in Fig. 7a. The patterns are characterized by steep slopes showing enrichment of light REE (LREE) relative to heavy REE (HREE) displayed by high $(La/Yb)_N$ ratio (8.3 to 20.5). Furthermore, the approximately parallel patterns may point to a genetic relationship between the samples and melt evolution via fractional crystallization. In this Figure, sample compositions are also compared with those of oceanic island basalt (OIB) and mid-ocean ridge basalts (MORB); enriched (E-) and normal (N-) MORBs (Sun and McDonough, 1989). As represented, the patterns of the studied samples are different from both N-MORB and E-MORB in terms of the ratio of LREE/HREE enrichment, while they coincide well with compositions of OIB. In the primitive mantle normalized multi-element diagram (Fig. 7b), except Y and HREEs other elements, including both the LILEs and HFSEs are enriched relative to N-MORB and E-MORB. Furthermore, the patterns do not show HFSE (like Nb and Ta) depletion. One of the points is that unlike OIB, some of the samples have K depletion, which could be due to secondary alteration or may have a petrogenetic implication.

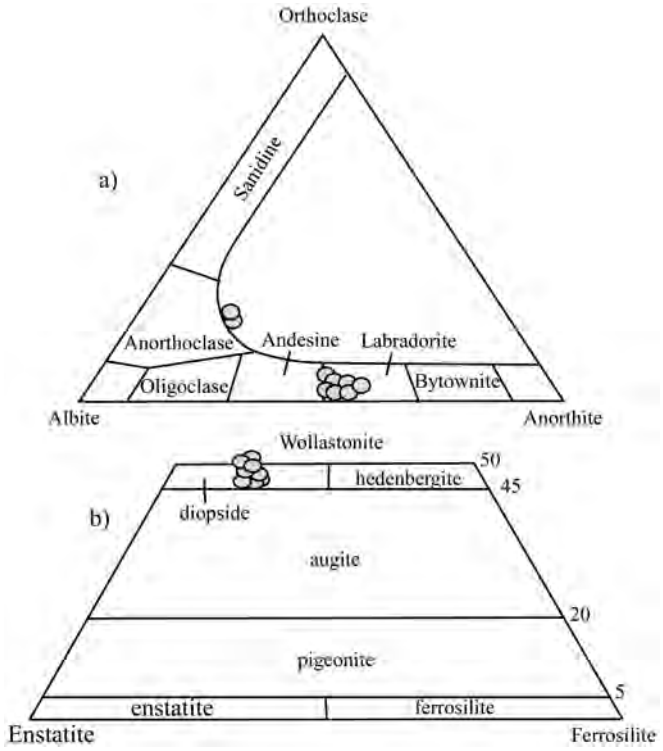

Fig. 4 - Mineral chemistry of the PVCA. (a) Albite-anorthite-orthoclase diagram showing the composition of plagioclase. (b) Pyroxene quadrilateral diagram showing clinopyroxene composition (Morimoto, 1989).

DISCUSSION

Mineral chemistry as a petrogenetic indicator

Chemical composition of the minerals can be used as a guide to deduce chemistry of the parental melt. In this regard, clinopyroxene composition has been used as a petrogenetic tool for discriminating magma series and tectonic setting of melt formation (Nisbet and Pearce, 1977; Beccaluva et al., 1989). High Ti content of clinopyroxene is a typical feature of alkaline basalts (Yoder and Tilley, 1962; Tracy and Robinson, 1977). In addition, Na_2O, CaO and Al_2O_3 are also higher in clinopyroxene composition of alkaline basalts compared to that of tholeiitic and calk-alkaline basalts. As these elements are incompatible during melting of a normal lherzolitic mantle (e.g., Pearce and Parkinson, 1993), their high concentration in the melt would suggest an enriched or undepleted mantle origin (e.g., Beccaluva et al., 1989; Cook et al., 2005) as well as low percent of partial melting, as expected for the mantle source of alkaline basalts. Clinopyroxene composition of basalts can also be used to discriminate various tectonic settings. In this regard, TiO_2, SiO_2, Al_2O_3, Na_2O, MgO, CaO and FeO contents of clinopyroxene are useful (Nisbet and Pearce, 1977; Leterrier et al., 1982; Beccaluva et al., 1989). In PVCA, the clinopyroxene composition clearly points to a within plate setting and alkaline nature of the parent melt (Fig. 8 a, b).

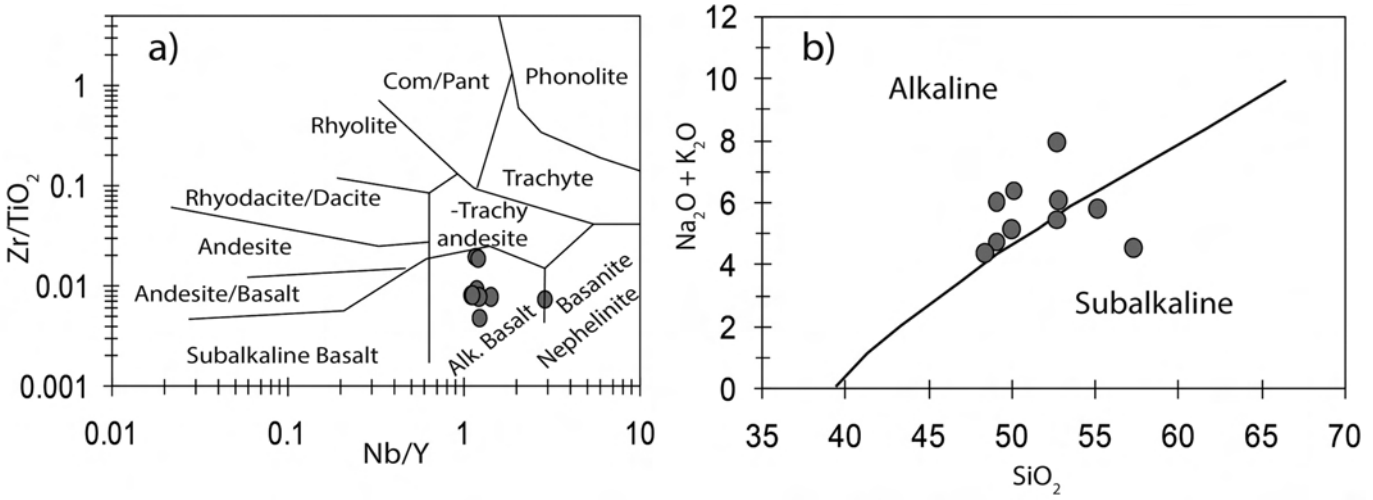

Fig. 5 - Chemical classification and magmatic series of the PVCA. (a) Zr/TiO_2 vs. Nb/Y classification diagram (Winchester and Floyd, 1977). (b) Total alkali ($Na_2O + K_2O$) vs. SiO_2 diagram (Irvine and Baragar, 1971).

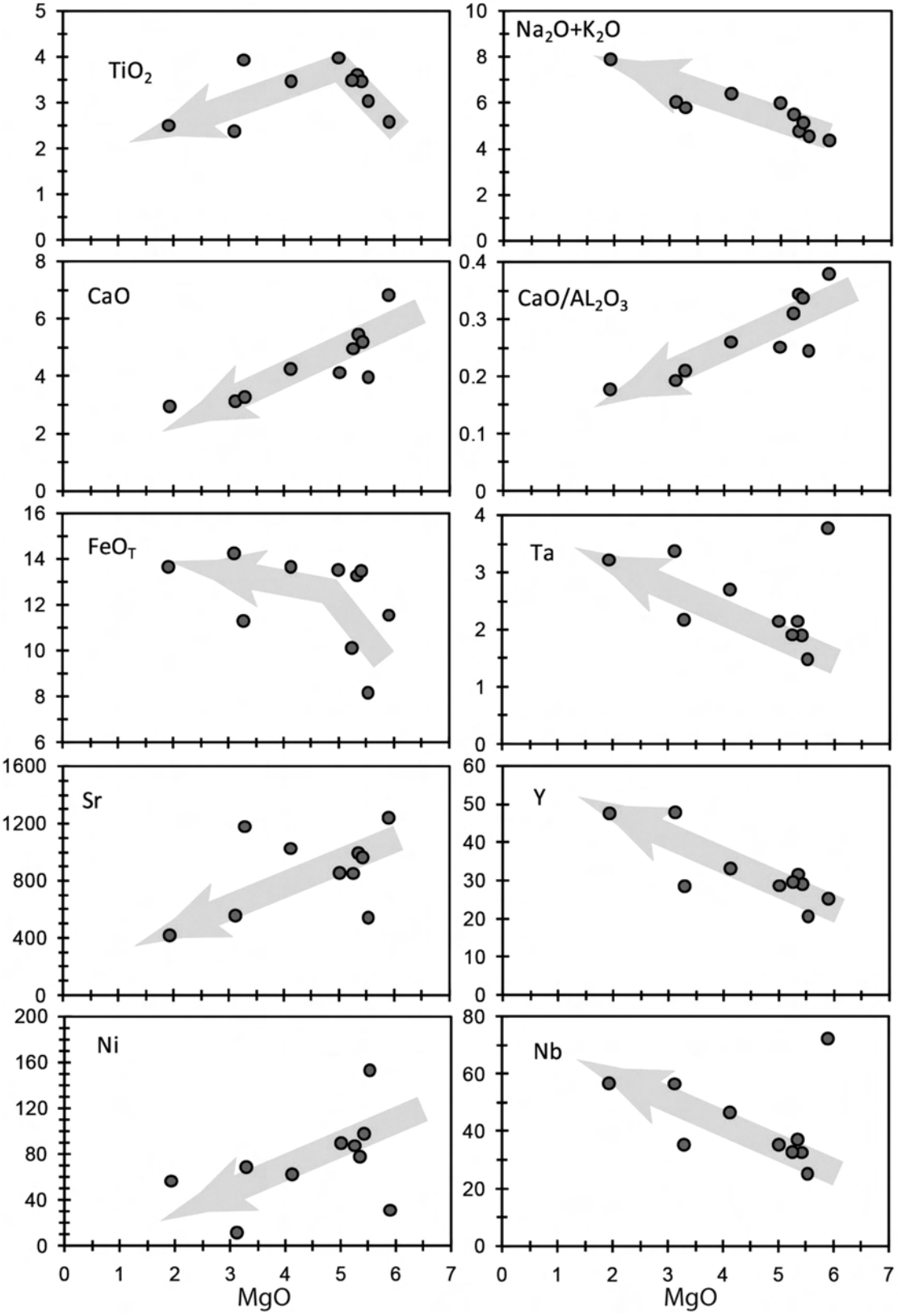

Fig. 6 - Major and trace elements vs. MgO variation diagrams for the studied rocks. Arrows indicate the inferred fractionation trends. Major element oxides are recalculated on anhydrous basis.

Table 1 - Representative analyses of clinopyroxenes from the PVCA.

Elements/ points (wt.%)	100	133	134	135	136	137	138	139	140	141	142	143
SiO_2	45.74	47.04	47.70	47.15	46.91	47.23	46.56	47.56	47.60	48.03	47.45	46.96
TiO_2	2.79	3.06	2.71	2.81	3.20	3.14	3.51	2.89	3.01	2.69	2.79	3.12
Al_2O_3	6.13	5.48	5.31	5.41	5.94	5.99	6.28	5.18	5.45	4.99	5.48	5.59
Cr_2O_3	0.00	0.00	0.06	0.00	0.00	0.00	0.00	0.03	0.02	0.04	0.00	0.03
Fe_2O_3	4.66	3.36	2.91	3.33	2.90	2.67	2.44	2.18	2.52	2.37	3.01	3.06
FeO	6.61	6.21	6.90	6.77	6.48	6.81	7.03	7.30	6.96	7.10	6.56	6.84
Mno	0.17	0.24	0.19	0.22	0.15	0.19	0.19	0.18	0.23	0.19	0.21	0.20
MgO	12.06	12.11	12.00	11.56	12.01	12.05	11.64	12.01	12.07	12.35	12.21	12.04
CaO	20.10	21.99	21.82	22.00	21.82	21.86	21.87	21.86	21.81	21.76	21.69	21.53
Na_2O	0.69	0.60	0.65	0.67	0.64	0.60	0.60	0.55	0.64	0.58	0.63	0.61
K_2O	0.00	0.00	0.00	0.00	0.00	0.01	0.02	0.00	0.00	0.00	0.00	0.02
Total	98.94	100.08	100.25	99.92	100.05	100.54	100.14	99.75	100.31	100.09	100.02	100.00
Si	1.74	1.77	1.79	1.78	1.76	1.76	1.75	1.79	1.78	1.80	1.78	1.77
Ti	0.08	0.09	0.08	0.08	0.09	0.09	0.10	0.08	0.08	0.08	0.08	0.09
Al	0.28	0.24	0.23	0.24	0.26	0.26	0.28	0.23	0.24	0.22	0.24	0.25
Cr	0.00	0.00	0.00	0.00	0.00	0.00	0.00	0.00	0.00	0.00	0.00	0.00
Fe^{3+}	0.13	0.10	0.08	0.09	0.08	0.07	0.07	0.06	0.07	0.07	0.09	0.09
Fe^{2+}	0.21	0.20	0.22	0.21	0.20	0.21	0.22	0.23	0.22	0.22	0.21	0.22
Mn	0.01	0.01	0.01	0.01	0.00	0.01	0.01	0.01	0.01	0.01	0.01	0.01
Mg	0.68	0.68	0.67	0.65	0.67	0.67	0.65	0.67	0.67	0.69	0.68	0.67
Ca	0.82	0.88	0.88	0.89	0.88	0.87	0.88	0.88	0.87	0.87	0.87	0.87
Na	0.05	0.04	0.05	0.05	0.05	0.04	0.04	0.04	0.05	0.04	0.05	0.04
K	0.00	0.00	0.00	0.00	0.00	0.00	0.00	0.00	0.00	0.00	0.00	0.00
Total	4.00	4.00	4.00	4.00	4.00	4.00	4.00	4.00	4.00	4.00	4.00	4.00
Wo	43.18	46.66	46.31	46.89	46.64	46.61	47.18	46.71	46.42	46.12	46.1	45.94
En	36.04	35.74	35.42	34.27	35.71	35.75	34.95	35.71	35.77	36.41	36.11	35.73
Fs	18.11	15.3	15.77	16.26	15.16	15.33	15.54	15.45	15.34	15.27	15.37	15.98

Wo- wollastonite; En- enstatite; Fs- ferrosilite.

Table 1 (*continued*)

Elements/Points (wt.%)	144	145	146	147	148	149	150	151	152	153	154	155	156	157	158
SiO_2	45.10	45.48	45.77	47.09	47.74	47.69	47.14	47.14	46.80	46.87	45.54	45.27	47.43	46.92	47.26
TiO_2	4.06	3.70	3.47	3.49	2.88	2.64	2.98	2.95	3.27	3.45	3.87	3.76	3.14	2.85	2.85
Al_2O_3	7.19	6.93	6.55	6.72	5.36	4.94	5.57	5.82	6.24	6.14	7.24	6.90	6.24	5.75	5.83
Cr_2O_3	0.02	0.00	0.00	0.00	0.00	0.00	0.00	0.00	0.00	0.07	0.03	0.00	0.00	0.00	0.05
Fe_2O_3	3.81	3.33	3.51	2.56	2.83	3.09	3.01	2.52	3.20	2.95	2.96	3.03	2.71	3.14	3.45
FeO	6.21	6.52	6.13	7.04	6.97	6.51	6.32	6.96	6.48	6.72	6.80	6.84	6.56	6.19	6.13
Mno	0.20	0.19	0.24	0.20	0.25	0.20	0.17	0.21	0.17	0.18	0.21	0.18	0.19	0.20	0.24
MgO	11.46	11.46	11.62	12.18	12.15	12.24	12.02	11.97	11.97	11.91	11.43	11.27	12.27	12.01	12.12
CaO	21.59	21.54	21.78	21.59	21.76	21.91	22.20	21.77	21.75	21.89	21.51	21.55	21.74	21.86	21.58
Na_2O	0.66	0.63	0.62	0.61	0.62	0.60	0.58	0.57	0.66	0.64	0.63	0.61	0.66	0.61	0.74
K_2O	0.00	0.02	0.00	0.00	0.00	0.01	0.00	0.00	0.00	0.01	0.03	0.00	0.00	0.01	0.01
Total	100.30	99.79	99.68	101.48	100.58	99.83	99.98	99.91	100.53	100.82	100.23	99.41	100.94	99.53	100.27
Si	1.70	1.72	1.73	1.74	1.78	1.79	1.77	1.77	1.75	1.75	1.71	1.72	1.76	1.77	1.77
Ti	0.11	0.10	0.10	0.10	0.08	0.07	0.08	0.08	0.09	0.10	0.11	0.11	0.09	0.08	0.08
Al	0.32	0.31	0.29	0.29	0.24	0.22	0.25	0.26	0.27	0.27	0.32	0.31	0.27	0.26	0.26
Cr	0.00	0.00	0.00	0.00	0.00	0.00	0.00	0.00	0.00	0.00	0.00	0.00	0.00	0.00	0.00
Fe^{3+}	0.11	0.09	0.10	0.07	0.08	0.09	0.09	0.07	0.09	0.08	0.08	0.09	0.08	0.09	0.10
Fe^{2+}	0.20	0.21	0.19	0.22	0.22	0.20	0.20	0.22	0.20	0.21	0.21	0.22	0.20	0.20	0.19
Mn	0.01	0.01	0.01	0.01	0.01	0.01	0.01	0.01	0.01	0.01	0.01	0.01	0.01	0.01	0.01
Mg	0.64	0.64	0.65	0.67	0.68	0.69	0.67	0.67	0.67	0.66	0.64	0.64	0.68	0.68	0.68
Ca	0.87	0.87	0.88	0.86	0.87	0.88	0.89	0.88	0.87	0.88	0.87	0.88	0.87	0.88	0.87
Na	0.05	0.05	0.05	0.04	0.05	0.04	0.04	0.04	0.05	0.05	0.05	0.04	0.05	0.04	0.05
K	0.00	0.00	0.00	0.00	0.00	0.00	0.00	0.00	0.00	0.00	0.00	0.00	0.00	0.00	0.00
Total	4.00	4.00	4.00	4.00	4.00	4.00	4.00	4.00	4.00	4.00	4.00	4.00	4.00	4.00	4.00
Wo	46.67	46.77	47.04	45.99	46.07	46.34	47.20	46.66	46.37	46.65	46.82	47.05	46.22	46.80	45.92
En	34.47	34.61	34.90	36.11	35.80	36.04	35.58	35.71	35.52	35.31	34.62	34.25	36.31	35.77	35.88
Fs	16.27	16.14	15.65	15.54	15.74	15.34	14.99	15.44	15.57	15.58	16.09	16.31	14.93	15.06	15.35

Wo- wollastonite; En- enstatite; Fs- ferrosilite.

Table 2 - Representative analyses of plagioclase from the PVCA.

Element/ poi (wt.%)	81	82	83	84	85	86	87	88	89	101	102	103	104
SiO_2	53.34	52.95	53.92	53.75	53.29	53.70	54.61	54.58	60.69	53.16	54.59	53.06	52.88
TiO_2	0.17	0.14	0.18	0.10	0.10	0.16	0.16	0.11	0.15	0.18	0.16	0.12	0.11
Al_2O_3	29.08	28.83	27.72	28.39	28.62	28.15	28.27	27.90	22.95	28.59	27.82	28.97	28.86
Cr_2O_3	0.00	0.01	0.00	0.10	0.03	0.00	0.02	0.00	0.00	0.01	0.00	0.00	0.00
FeO	0.64	0.60	0.61	0.61	0.60	0.69	0.58	0.55	1.62	0.76	0.87	0.76	0.74
MnO	0.01	0.00	0.00	0.00	0.00	0.01	0.00	0.00	0.00	0.02	0.00	0.06	0.00
MgO	0.09	0.07	0.08	0.06	0.07	0.07	0.07	0.07	0.30	0.04	0.16	0.04	0.08
CaO	11.11	10.92	9.94	10.52	10.74	10.46	10.20	9.94	3.61	10.83	9.63	11.05	10.95
Na_2O	4.62	4.78	5.18	4.82	4.88	5.05	5.12	5.13	5.84	5.01	4.98	4.70	4.79
K_2O	0.64	0.61	0.70	0.71	0.66	0.63	0.72	0.71	3.59	0.54	0.77	0.55	0.59
Total	99.70	98.92	98.32	99.06	98.99	98.92	99.74	98.99	98.75	99.14	98.97	99.30	98.99
Si	2.43	2.43	2.48	2.46	2.44	2.46	2.48	2.49	2.76	2.43	2.49	2.43	2.43
Ti	0.01	0.00	0.01	0.00	0.00	0.01	0.01	0.00	0.01	0.01	0.01	0.00	0.00
Al	1.56	1.56	1.50	1.53	1.55	1.52	1.51	1.50	1.23	1.54	1.50	1.56	1.56
Fe^{2+}	0.02	0.02	0.02	0.02	0.02	0.03	0.02	0.02	0.06	0.03	0.03	0.03	0.03
Mn	0.00	0.00	0.00	0.00	0.00	0.00	0.00	0.00	0.00	0.00	0.00	0.00	0.00
Mg	0.01	0.01	0.01	0.00	0.00	0.00	0.00	0.00	0.02	0.00	0.01	0.00	0.01
Ca	0.54	0.54	0.49	0.52	0.53	0.51	0.50	0.49	0.18	0.53	0.47	0.54	0.54
Na	0.41	0.42	0.46	0.43	0.43	0.45	0.45	0.45	0.52	0.44	0.44	0.42	0.43
K	0.04	0.04	0.04	0.04	0.04	0.04	0.04	0.04	0.21	0.03	0.04	0.03	0.03
Total	5.01	5.02	5.01	5.01	5.02	5.02	5.01	5.00	4.98	5.03	5.00	5.01	5.02
Ab %	41.32	42.61	46.54	43.42	43.40	44.89	45.62	46.27	57.28	44.15	46.07	42.09	42.65
An %	54.89	53.82	49.33	52.40	52.76	51.42	50.18	49.53	19.55	52.74	49.24	54.68	53.91
Or %	3.79	3.57	4.13	4.19	3.84	3.69	4.20	4.20	23.16	3.11	4.69	3.23	3.44

Ab- albite; An- anorthite; Or- orthoclase.

Table 3 - Whole rock major and trace element analyses of the PVCA.

Samples	MDB-32	MDB-30	MDB-28	MDB-27	MDB-20	MDB-19	MDB-16	MDB-15	MDB-13	MDB-11
Latitude- N	36°12′30"	36°12′15"	36°12′14"	36°13′35"	36°13′29"	36°13′33"	36°13′42"	36°13′36"	36°13′59"	36°13′47"
Longitude- E	51°19′48"	51°20′40"	51°20′45"	51°42′49"	51°42′21"	51°42′14"	51°42′17"	51°42′10"	51°42′29"	51°42′53"
XRF (wt.%)										
SiO_2	48.01	54.26	45.7	50.72	47.92	51.4	53.46	47.08	49.62	45.07
TiO_2	3.45	3.01	3.62	2.35	3.44	2.51	3.93	3.98	3.48	2.56
Al_2O_3	15.69	15.35	14.77	15.49	14.74	16.16	15.14	15.75	15.03	16.8
Fe_2O_3	1.8	1.08	1.75	1.88	1.77	1.8	1.49	1.78	1.33	1.53
FeO	11.99	7.17	11.7	12.53	11.83	11.99	9.93	11.87	8.88	10.18
MnO	0.16	0.15	0.25	0.19	0.22	0.15	0.13	0.17	0.16	0.1
MgO	3.95	5.23	4.98	2.99	5.19	1.88	3.18	4.81	4.94	5.49
CaO	4.08	3.75	5.07	3	4.97	2.87	3.18	3.96	4.66	6.36
Na_2O	4.4	3.52	4.1	5.43	4.38	7.6	4.97	5.22	4.72	3.42
K_2O	1.74	0.75	0.34	0.37	0.54	0.11	0.63	0.53	0.43	0.62
P_2O_5	0.62	0.31	0.9	1.08	0.78	1.04	0.87	0.87	0.78	0.98
LOI	3.54	5.14	6.59	2.96	3.43	1.84	2.41	3.35	5.23	6.21
Total	99.44	99.73	99.77	98.99	99.2	99.34	99.33	99.37	99.26	99.33
Mg#	34.11	53.35	40.06	27.25	40.79	19.72	33.48	38.87	46.61	45.86
XRF(ppm)										
Zn	195	108	167	212	160	194	126	190	151	125
Cu	48	114	86	41	62	49	46	144	135	39
Sc	16	27	21	16	18	18	19	20	22	10
Ga	31	24	26	31	25	28	22	27	24	24
Ni	29	155	81	2	96	5	60	74	90	30
Co	49	64	48	34	49	32	40	52	44	35
Cr	0	219	48	0	75	0	11	8	80	10
V	186	205	199	91	196	89	199	202	189	126
Rb	44	14	6	7	8	4	9	9	8	8
Ba	676	182	141	133	290	104	282	240	156	892
Nb	49	28	42	59	36	59	35	37	36	76
Sr	1054	560	1028	570	976	417	1174	865	873	1283
Nd	53	23	45	69	43	63	44	44	43	58
Zr	296	169	375	529	306	519	324	333	315	225
Y	40	26	39	56	35	55	32	33	35	30
Hf	9	6	5	13	8	9	9	8	5	6

Mg# = 100 × Mg/(Mg + Fe^{2+}).

Melting condition and source mineralogy

The studied samples are chemically different from N-MORB and E-MORB but similar to OIB (Fig. 7a, b). Indeed, these characters are inherited from the melt source and melting conditions. Low percent partial melting of a deep garnet lherzolitic mantle will produce an OIB-like melt (e.g., Fitton, 2007; Humphreys and Niu, 2009; Davis et al., 2011). Based on chemical modeling it is possible to deduce mineralogy and depth of mantle origin. In this regard, trace element data, particularly REE abundances are good indicators because they are sensitive to partial melting conditions such as melting pressure and nature of the Al-bearing phase (spinel or garnet) in the mantle. Here, chemical modeling using La/Yb and Gd/Yb ratios is presented (Fig. 9) showing that the studied samples are consistent with either an enriched or undepleted mantle (bulk silicate earth) source. Moreover, these ratios indicate a low degree of partial melting (< 10%) in high pressure (~ 4 GPa) conditions, which accords with more than 100 km mantle depth. As expected, this garnet peridotite mantle source is chemically different from a depleted N-MORB source mantle (spinel peridotite). Similar results have been obtained using other trace element abundances. For example, Sm/Yb vs. La/Yb or Zr/Y vs. La/Sm variations (not shown) imply partial melting of around 10% from a garnet peridotite source (~ 20% garnet in the mantle). Low melting degrees and deep source conditions can also be inferred from major element chemistry of the studied samples, i.e., high FeO and TiO_2 and low CaO values (Mertz et al., 2001; Table 3).

Mantle source characteristics

As explained previously, the samples are chemically identical to oceanic island basalts (OIB). Based on isotopic signatures, OIB can be classified into isotopically distinct groups: HIMU (or high μ), enriched mantle (EMI) and EMII (White, 1985; Zindler and Hart, 1986). In terms of

Table 3 (*continued*)

Samples	MDB-32	MDB-30	MDB-28	MDB-27	MDB-20	MDB-19	MDB-16	MDB-15	MDB-13	MDB-11
LA-ICP-MS (ppm)										
Cs	0.369	1.368	1.197	0.464	0.262	0.06	0.283	0.158	0.509	0.748
Ba	669	164	140	121	271	100	270	226	157	849
Rb	38.96	12.64	4.36	5.81	7.22	1.26	8.63	7.83	6.61	7.85
Sr	1024	540	990	554	965	416	1177	856	851	1241
Y	33.1	20.7	31.7	48.0	29.2	47.6	28.7	28.7	29.8	25.3
Zr	277	155	344	490	287	492	330	315	297	207
Nb	46.8	25.1	37.3	56.7	32.7	56.8	35.4	35.3	32.9	72.6
La	39.22	16.87	35.34	47.89	30.04	49.55	32.91	27.37	33.58	57.02
Ce	84.73	39.10	79.05	115.94	67.34	117.01	72.93	64.39	72.14	107.28
Pr	10.61	4.87	10.26	15.21	8.78	15.59	9.50	8.85	9.16	11.78
Nd	46.29	22.17	44.06	67.09	38.72	66.85	41.28	39.56	40.46	45.87
Sm	10.44	5.56	9.46	15.82	8.55	14.97	9.70	8.88	8.99	7.97
Eu	3.459	1.973	3.844	5.06	3.101	5.057	3.331	3.462	3.223	2.764
Gd	10.33	5.53	9.51	14.16	8.16	13.79	9.00	8.62	8.68	6.64
Tb	1.329	0.857	1.256	1.864	1.074	1.869	1.214	1.151	1.229	0.927
Dy	7.571	4.509	7.147	10.514	6.271	10.568	6.698	6.406	6.613	5.331
Ho	1.331	0.784	1.267	1.851	1.163	1.811	1.206	1.113	1.165	0.936
Er	3.07	2.099	3.054	4.555	2.821	4.582	2.934	2.865	2.764	2.522
Tm	0.39	0.245	0.368	0.544	0.349	0.548	0.359	0.329	0.359	0.333
Yb	2.278	1.458	2.364	3.52	2.216	3.656	1.977	2.039	2.326	1.993
Lu	0.355	0.202	0.305	0.473	0.281	0.526	0.309	0.291	0.289	0.277
Hf	7.26	4.23	7.96	11.82	6.89	11.49	8.14	7.33	7.17	4.90
Ta	2.70	1.47	2.14	3.37	1.89	3.21	2.17	2.14	1.90	3.77
Th	4.42	2.54	3.26	6.72	2.98	6.81	2.87	2.85	3.03	6.71
U	1.063	0.542	0.968	1.649	0.836	1.658	0.695	0.758	0.77	1.387
Sc	17.46	26.05	20.31	16.30	21.07	17.07	20.58	20.03	22.01	10.74
V	189	206	199	94	201	98	199	207	188	128
Cr	28.697	226	63.8	17.2	101	22.7	27.5	30.2	89.6	26.6
Co	45.3	57.3	42.7	29.7	43.3	28.1	35.6	47.5	38.8	29.4
Cu	38.7	94.6	70.5	31.9	51.7	38.3	34.3	113.4	110.5	29.2
Pb	2.647	1.755	4.165	4.306	3.639	5.38	5.213	7.029	3.714	3.345
Zn	142	79	127	157	123	153	108	148	110	91
Ga	24.3	19.7	22.8	26.4	20.9	23.6	18.0	22.8	20.2	18.5
$(La/Sm)_N$	2.43	1.96	2.41	1.95	2.27	2.14	2.19	1.99	2.41	4.62
$(Sm/Yb)_N$	5.09	4.23	4.45	4.99	4.28	4.55	5.45	4.84	4.29	4.44
$(La/Yb)_N$	12.35	8.3	10.72	9.76	9.72	9.72	11.94	9.63	10.36	20.52
Ba/La	17.24	10.77	3.99	2.77	9.67	2.1	8.56	8.75	4.65	15.64
Zr/Nb	5.93	6.16	9.22	8.63	8.78	8.65	9.32	8.92	9.01	2.85
La/Nb	0.84	0.67	0.95	0.84	0.92	0.87	0.93	0.78	1.02	0.79
Ba/Nb	14.45	7.23	3.78	2.34	8.88	1.83	7.96	6.78	4.74	12.29
Ba/Th	153	71.6	43.2	19.7	97.5	15.3	98.1	83.9	51.5	132.9
Rb/Nb	0.83	0.5	0.12	0.1	0.22	0.02	0.24	0.22	0.2	0.11
K/Nb	322	263	82	57	143	17	153	129	115	76
Th/Nb	0.09	0.1	0.09	0.12	0.09	0.12	0.08	0.08	0.09	0.09

some trace element contents, these groups can also be differentiated such that HIMU basalts relative to EM basalts are depleted in Rb, Ba, Th, K, U and Pb and enriched in Nb and Ta. Furthermore, some trace element ratios, including Zr/Nb, La/Nb, Ba/Nb, Ba/Th, Rb/Nb, K/Nb, Th/Nb, Th/La and Ba/La are useful in this regard (e.g., Weaver, 1991; Mertz et al., 2001; Cook et al., 2005). In Fig. 10, although in the Zr/Nb vs. K/Nb variation diagram the data points are scattered among different fields, in the La/Nb, Ba/Nb and Th/Nb vs. K/Nb diagrams the values are more akin to those of HIMU and EMII. Discrimination between HIMU and EM is also possible using other factors such as Rb content or K/La and Nb/Rb ratios. In HIMU basalts, K/La (< 260) and Rb (< 30 ppm) are lower than those of EM basalts having higher K/La (> 260) or Rb (> 30 ppm) (Willbold and Stracke, 2006). In PVCA, the mean value of K/La and Rb is 164 and 10 ppm, respectively, which is more comparable with HIMU values. In addition, the

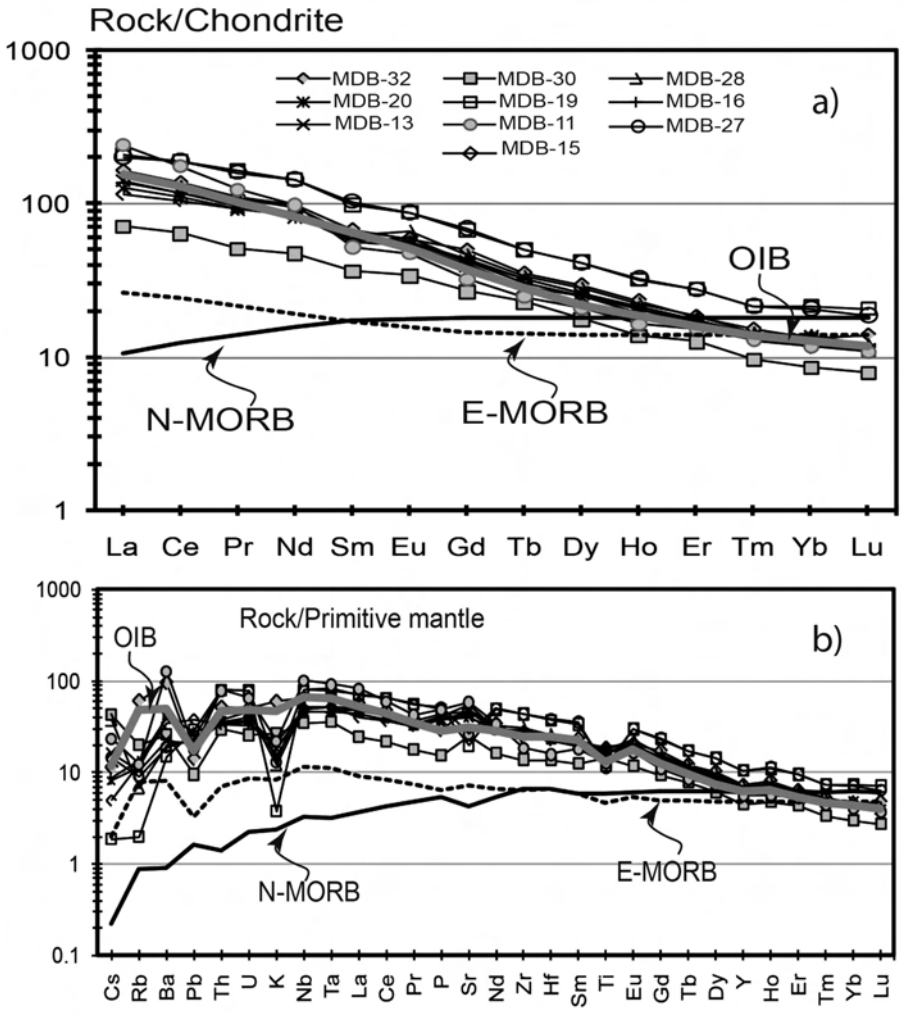

Fig. 7 - (a) Chondrite-normalized rare earth element (REE) patterns and (b) Primitive mantle-normalized multi-element patterns for the PVCA. E-MORB: Enriched MORB; N-MORB: Normal- MORB and OIB: Oceanic Island Basalt. Normalizing values after Sun and McDonough (1989).

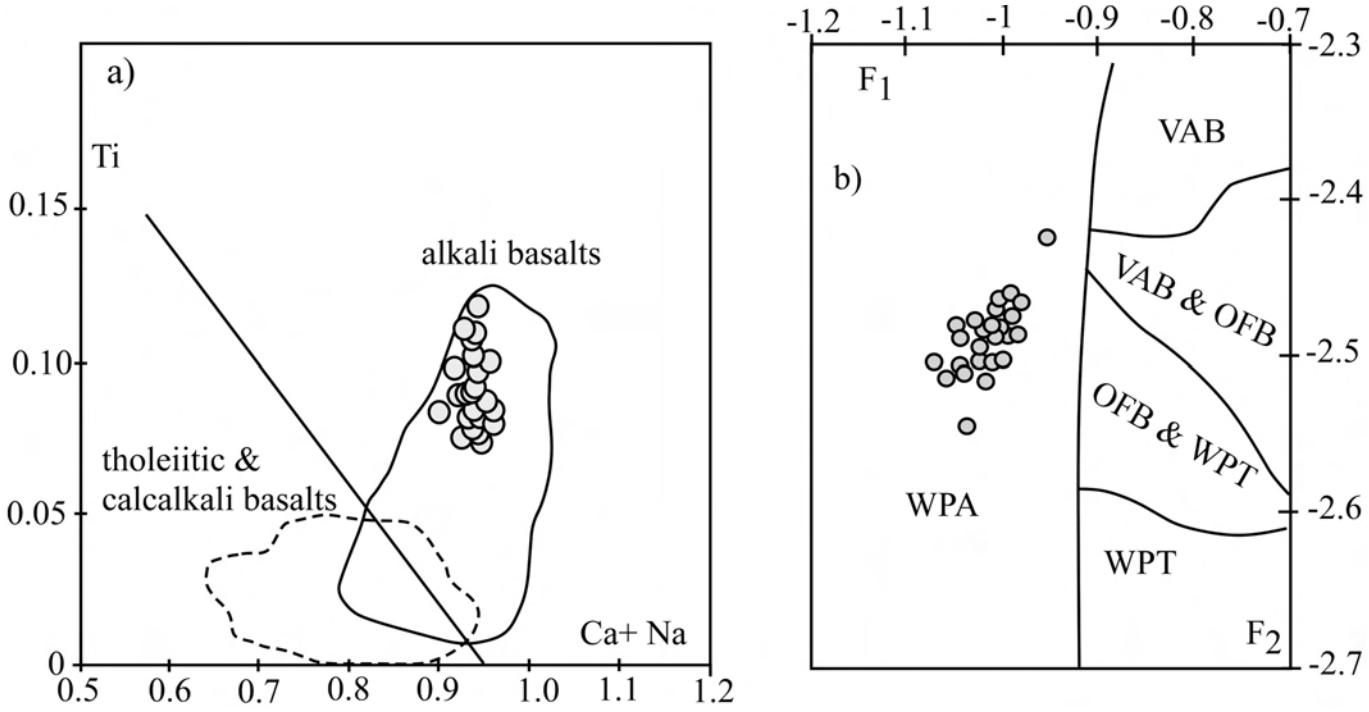

Fig. 8 - Discrimination diagrams based on clinopyroxene composition. (a) Ti vs. Ca + Na diagram (Leterrier et al., 1982). (b) F_1 vs. F_2 diagram (Nisbet and Pearce, 1977). VAB- volcanic arc basalt; OFB- ocean floor basalt; WPT- within plate tholeiite; WPA- within plate alkaline. $F_1 = -0.012 \times SiO_2 - 0.0807 \times TiO_2 + 0.0026 \times A1_2O_3 - 0.0012 \times FeO^* - 0.0026 \times MnO + 0.0087 \times MgO - 0.0128 \times CaO - 0.0419 \times Na_2O$. $F_2 = -0.0469 \times SiO_2 - 0.0818 \times TiO_2 - 0.0212 \times A1_2O_3 - 0.0041 \times FeO^* - 0.1435 \times MnO - 0.0029 \times MgO + 0.0085 \times CaO + 0.0160 \times Na_2O$.

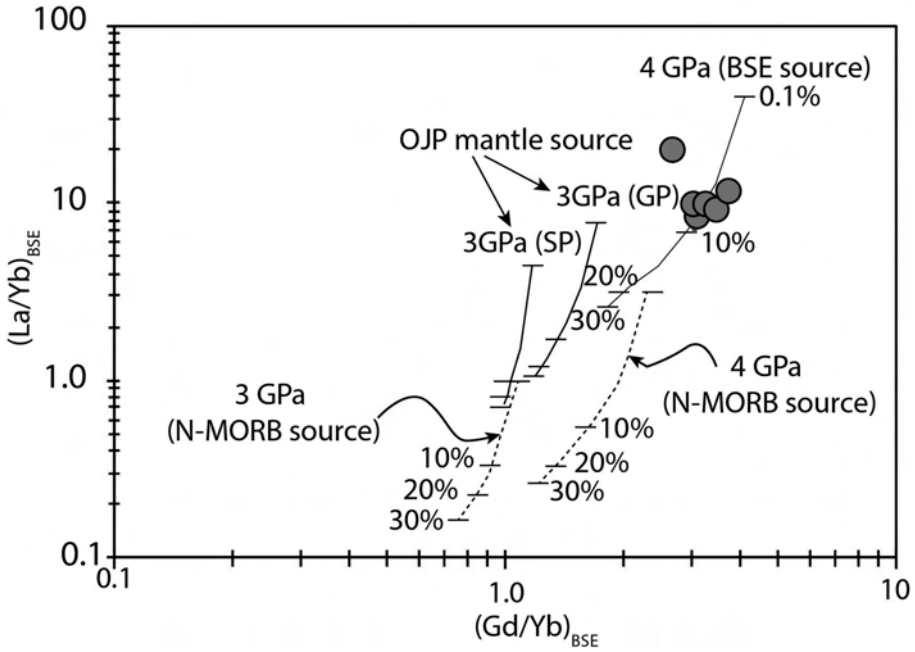

Fig. 9 - La/Yb vs. Gd/Yb diagram comparing REE composition of the PVCA with calculated trends of non-modal batch partial melts produced from different mantle sources. Details of the modeling including various mantle source characteristics and distribution coefficients are given by Reichow et al. (2005).

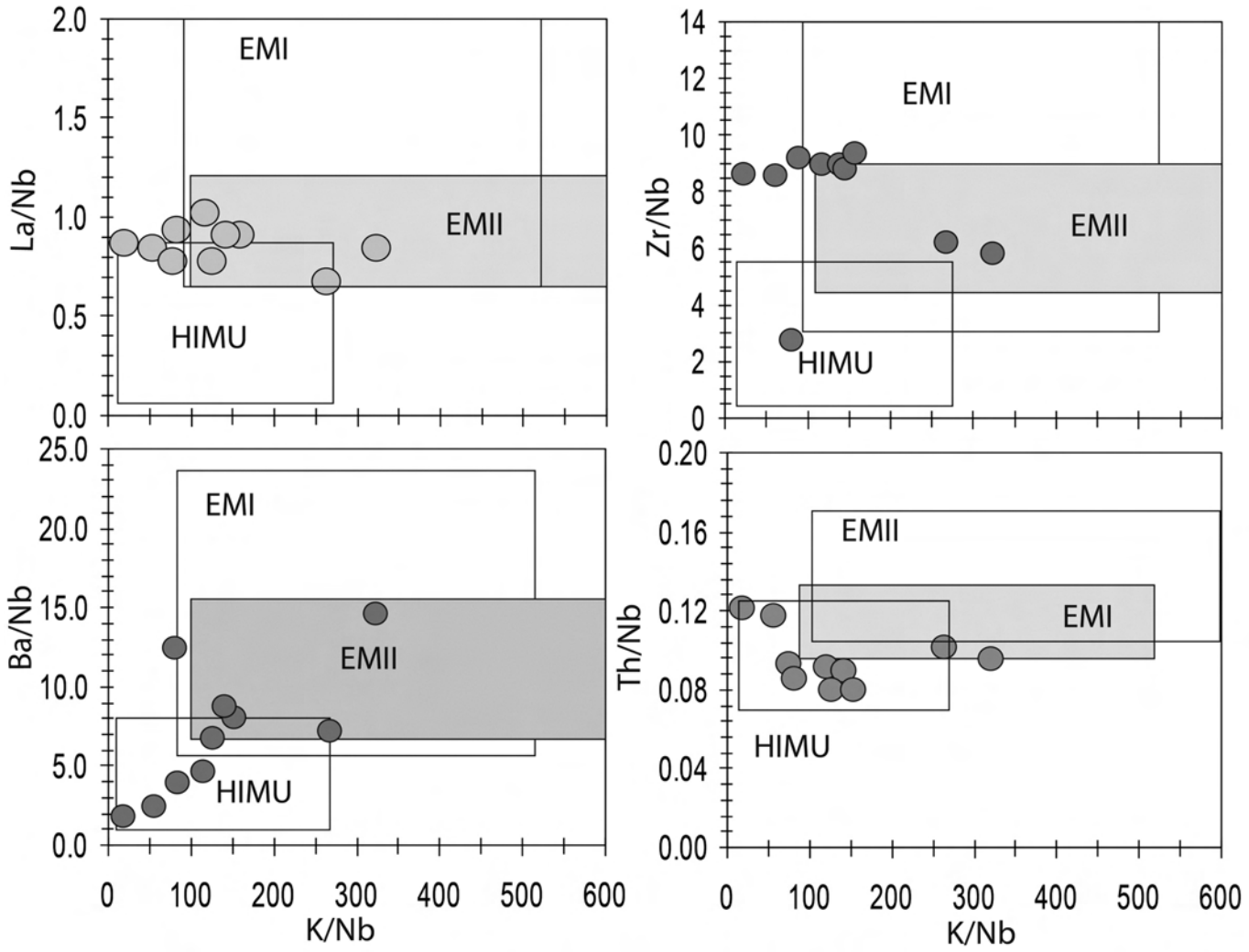

Fig. 10 - Variation of La/Nb, Zr/Nb, Ba/Nb and Th/Nb vs. K/Nb representing geochemical features of the mantle sources for the studied volcanics. The fields of EMI, EMII and HIMU mantle reservoirs are taken from Cook et al. (2005).

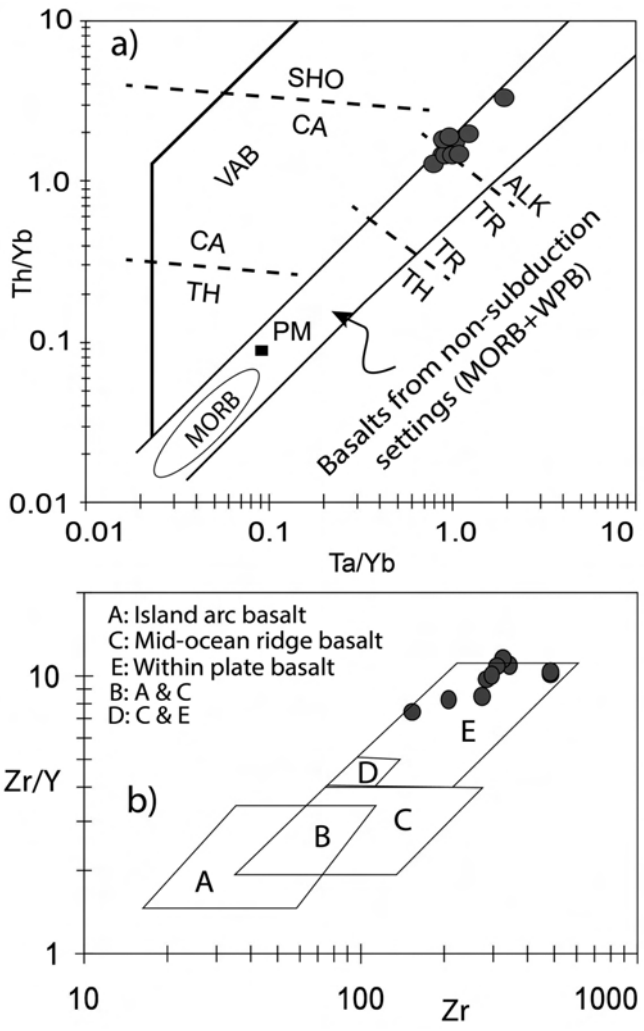

Fig. 11 - (a) Th/Yb vs. Ta/Yb diagram (Pearce, 1982) and (b) Zr/Y vs. Zr diagram (Pearce and Norry, 1979) showing a non-subduction, within-plate tectonic setting for the studied rocks. Abbreviations: ALK- alkaline; CA- calk-alkaline; PM- primitive mantle; SHO- shoshonitic; TH- tholeiitic; TR- transitional; VAB- volcanic arc basalt; WPB- within-plate basalt.

Nb/Rb ratio is different in HIMU (> 2.5) and EM melts (< 1.5; Willbold and Stracke, 2006). The mean value of Nb/Rb ratio in PVCA is 9.4. K depletion in Fig. 7b, is another common feature of HIMU basalts (Chauvel et al., 1992). Therefore, trace elements as well as some major element geochemical characteristics of PVCA are more similar to HIMU melts. However, it should be noted that some elements such as Rb and K are mobile and susceptible to secondary alteration processes.Thus, their concentration must be treated with caution.

Tectonic setting

In Fig. 7b, the lack of HFSE negative anomalies is an obvious difference between the studied rocks and subduction zone melts. Moreover, the Th/Yb vs. Ta/Yb variation (Fig. 11a; Pearce, 1982; 1983) suggests non-subduction related setting for PVCA. Also, on the basis of other HFSEs, e.g., Zr or Zr/Y contents, the samples display a within plate setting (Fig. 11b).

According to many researchers, Paleotethys had a north-dipping subduction zone (e.g., Alavi, 1991; Stampfli, 2000; Gaetani et al., 2009; Zanchi et al., 2009). In contrast, another viewpoint considers south-dipping subduction underneath Cimmerian terranes. Şengör (1990) believes that during Carboniferous and Early Permian, the northeast margin of Gondwana, including the Podataksasi Zone in the west, the Alborz and Tabas regions in the Middle, and the Central Pamirs in the east recorded an active continental margin magmatism. In agreement with this idea, Ruban et al. (2007) stated that the mid-Carboniferous angular unconformity in the Arabian region could be the result of Paleotethyan subduction beneath the north Gondwanian margin. Based on our findings, the geochemical characteristics of Alborz Permian volcanism are consistent with continental intra-plate magmatism without any subduction zone signatures. As a result, it could be argued that during Permian, Alborz was a passive continental margin to the south of Paleotethys. This hypothesis implies the northward subduction of Paleotethys beneath the Eurasian margins, and not a

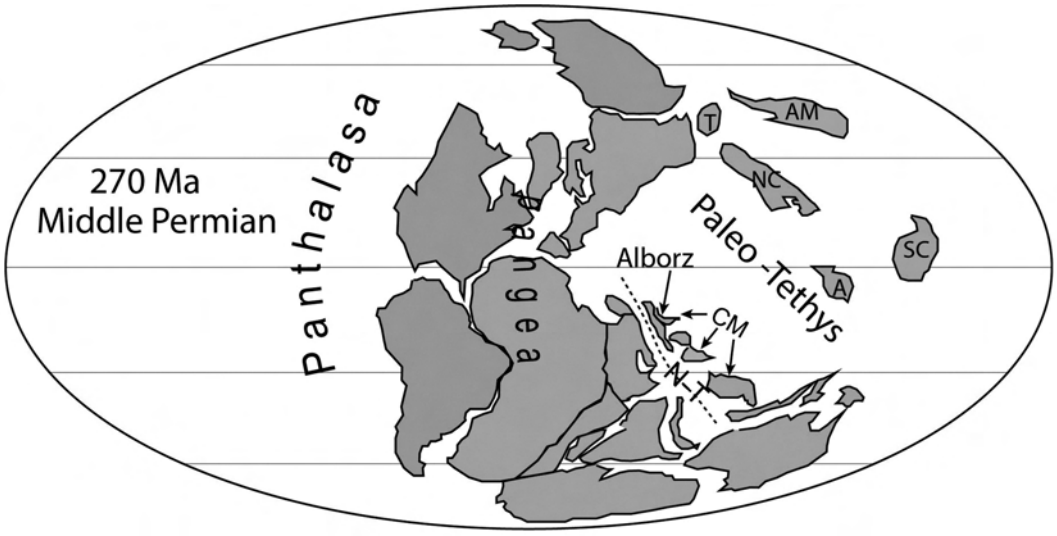

Fig. 12 - Paleogeographic reconstruction and plate boundaries in Middle Permian (270 Ma), showing location of Alborz and other Cimmerian micro-continents (CM). Redrawn from Domeier and Torsvik (2014). Abbreviation, A- Annamia; AM- Amuria; NC- North China; N-T- Neotethys Ocean; SC- South China; T- Tarim.

southward subduction beneath the Cimmerian or at least the Alborz microplate.

Contemporaneous Permian magmatism also occurred in some other areas, including the Tianshan and Tarim basin of northwestern China (Yang et al., 2007; Zhou et al., 2009; Zhang et al., 2010a; 2010b; Yu et al., 2011), Oman and North Africa (Wilson et al., 1998; Maury et al., 2003; Lapierre et al., 2004) and South Tibet (Garzanti et al., 1999). Additionally, the Siberian extensive basaltic volcanism has been considered as a possible reason for the end-Permian mass extinction (Renne et al., 1995; Reichow et al., 2009). In northwestern and southeastern China, Permian volcanism has been linked to mantle plume activity (Xu et al., 2001; Zhou et al., 2009; Zhang et al., 2010a; Yu et al., 2011). However, in Alborz, the low volume of the studied volcanics is not comparable to typical plume-related volcanic eruptions. During Middle-Late Permian, Alborz was part of the Cimmerian terranes separated from Gondwana via the opening of Neotethys (e.g., Muttoni et al., 2009; Angiolini et al., 2013). The Alborz Permian magmatism was plausibly triggered by an extensional tectonic regime and continental rift events. Stratigraphic evidence showing deepening of sedimentary basins during Permian time is consistent with extensional tectonic activity. In addition, other Gondwana-derived fragments of Iran exemplify records of extensional magmatism during the Permian (Berberian and King, 1981).

CONCLUSION

Basaltic flows of Central Alborz (northeast of Baladeh-Siahbisheh) crop out between Middle-Late Permian formations. Based on mineral and whole rock chemistry, the samples display an alkaline nature. Furthermore, they show OIB chemical characteristics resulting from a low degree partial melting of a garnet-bearing mantle source. As the rocks do not show subduction zone geochemical signatures, it can be stated that during Permian, the Alborz area was a passive continental margin in the southern border of Paleotethys, and its magmatism was probably triggered by an extensional tectonic regime contemporaneous with the early development of Neotethys.

ACKNOWLEDGMENTS

We thank the Kharazmi University for well organized support during field work. Professor S. Amini is gratefully acknowledged for his help doing microprobe analyses. We would also like to thank Andrea Zanchi and an anonymous referee for providing very helpful comments and constructive criticisms of an earlier version of the manuscript.

REFERENCES

Alavi M., 1991. Sedimentary and structural characteristics of the Paleo-Tethys remnants in northeastern Iran. Geol. Soc. Am. Bull., 103: 983-992.

Alavi M., 1996. Tectonostratigraphic synthesis and structural style of the Alborz Mountain system in Northern Iran. J. Geodyn., 21: 1-33.

Allen M., Ghassemi M., Shahrabi M. and Qorashi M., 2003. Accommodation of Late Cenozoic oblique shortening in the Alborz range, northern Iran. J. Struct. Geol., 25: 659-672.

Angiolini L., Crippa G., Muttoni G. and Pignatti J., 2013. Guadalupian (Middle Permian) paleobiogeography of the Neotethys Ocean. Gondw. Res., 24: 173-184.

Beccaluva L., Macciotta G., Piccardo G.B. and Zeda O., 1989. Clinopyroxene composition of ophiolite basalts as petrogenetic indicator. Chem. Geol., 77: 165-182.

Berberian M. and King G.C.P., 1981. Towards a paleogeography and tectonic evolution of Iran. Can. J. Earth Sci., 18: 210-265.

Chauvel C., Hofmann A.W. and Vidal P., 1992. HIMU-EM: The French Polynesian connection. Earth Planet. Sci. Lett., 110: 99-119.

Cook C., Briggs R.M., Smith, I.E.M. and Maas R., 2005. Petrology and geochemistry of intraplate basalts in the South Auckland Volcanic Field, New Zealand: Evidence for two coeval magma suites from distinct sources. J. Petrol., 46: 473-503.

Davis F.A., Hirschmann M.M. and Humayun M., 2011. The composition of the incipient partial melt of garnet peridotite at GPa and the origin of OIB. Earth Planet. Sci. Lett., 308: 380-390.

Domeier M. and Torsvik T.H., 2014. Plate tectonics in the late Paleozoic. Geosci. Front., 5: 303-350.

Fitton J.G., 2007. The OIB paradox. Geol. Soc. Am. Spec. Pap., 430: 387-412.

Gaetani M., Angiolini L., Ueno K., Nicora A., Stephenson M.H., Sciunnach D., Rettori R., Price G.D. and Sabouri J., 2009. Pennsylvanian-Early Triassic stratigraphy in the Alborz Mountains (Iran). Geol. Soc. London Spec. Publ., 312: 79-128.

Garzanti E., Le Fort P. and Sciunnach D., 1999. First report of Lower Permian basalts in South Tibet: tholeiitic magmatism during break-up and incipient opening of Neotethys. J. Asian Earth Sci., 17: 533-546.

Golonka J., 2004. Plate tectonic evolution of the southern margin of Eurasia in the Mesozoic and Cenozoic. Tectonophysics, 381: 235-273.

Golonka J., 2007. Late Triassic and Early Jurassic palaeogeography of the world. Palaeo. Palaeo. Palaeo., 244: 297-307.

Guillong M., Meier D., Allan M., Heinrich C. and Yardley B., 2008. SILLS: a MATLAB-based program for the reduction of laser ablation ICP-MS data of homogeneous materials and inclusions. Mineral. Ass. Can. Short Course, 40: 328-333.

Günther D., 2002. Laser-ablation inductively-coupled plasma mass spectrometry. Anal. Bioanal. Chem., 372: 31-32.

Humphreys E.R. and Niu Y., 2009. On the composition of ocean island basalts (OIB): The effects of lithospheric thickness variation and mantle metasomatism. Lithos, 112: 118-136.

Irvine T.N. and Baragar W.R.A., 1971. A guide to the chemical classification of the common volcanic rocks. Can. J. Earth Sci., 8: 523-548.

Lapierre H., Samper A., Bosch D., Maury R.C., Béchennec F., Cotten J., Demant A., Brunet P., Keller F. and Marcoux J., 2004. The Tethyan plume: geochemical diversity of Middle Permian basalts from the Oman rifted margin. Lithos, 74: 167-198.

Leterrier J., Maury R.C., Thonon P., Girard D. and Marchal M., 1982. Clinopyroxene composition as a method of identification of the magmatic affinities of paleo-volcanic series. Earth Planet. Sci. Lett., 59: 139-154.

Maury R.C., Béchennec F., Cotten J., Caroff M., Cordey F. and Marcoux J., 2003. Middle Permian plume-related magmatism of the Hawasina Nappes and the Arabian Platform: Implications on the evolution of the Neotethyan margin in Oman. Tectonics, 22: 1073.

Mertz D.F., Weinrich A.J., Sharp W.D. and Renne P.R., 2001. Alkaline intrusions in a near-trench setting, Franciscan Complex, California: Constraints from geochemistry, petrology, and $^{40}Ar/^{39}Ar$ chronology. Am. J. Sci., 301: 877-911.

Morimoto N., 1989. Nomenclature of pyroxenes. Can. Mineral., 27: 143-156.

Muttoni G., Gaetani M., Kent D.V., Sciunnach D., Angiolini L., Berra F., Garzanti E., Mattei M. and Zanchi A., 2009. Opening of the Neo-Tethys Ocean and the Pangea B to Pangea A transformation during the Permian. GeoArabia, 14: 17-48.

Nisbet E. and Pearce J., 1977. Clinopyroxene composition in mafic lavas from different tectonic settings. Contrib. Mineral. Petrol., 63: 149-160.

Pearce J.A., 1982. Trace element characteristics of lavas from destructive plate boundaries. In: R.S. Thorpe (Ed.), Andesites. John Wiley & Sons, New York, p. 525-548.

Pearce J.A., 1983. Role of the subcontinental lithosphere in magma genesis at active continental margins. In: C.J. Hawkesworth and M.J. Norry (Eds.), Continental basalts and mantle xenoliths. Shiva, Nantwich, p. 230-249.

Pearce J. and Norry M., 1979. Petrogenetic implications of Ti, Zr, Y, and Nb variations in volcanic rocks. Contrib. Mineral. Petrol., 69: 33-47.

Pearce J.A. and Parkinson. I.J., 1993. Trace element models for mantle melting: application to volcanic arc petrogenesis. Geol. Soc. London Spec. Publ., 76: 373-403.

Reichow M.K., Pringle M.S., Al'Mukhamedov A.I., Allen M.B., Andreichev V.L., Buslov M.M., Davies C.E., Fedoseev G.S., Fitton J.G., Inger S., Medvedev A.Y., Mitchell C., Puchkov V.N., Safonova I.Y., Scott R.A. and Saunders A.D., 2009. The timing and extent of the eruption of the Siberian Traps large igneous province: Implications for the end-Permian environmental crisis. Earth Planet. Sci. Lett., 277: 9-20.

Reichow M.K., Saunders A.D., White R.V., Al'Mukhamedov A.I. and Medvedev A.Y., 2005. Geochemistry and petrogenesis of basalts from the West Siberian Basin: an extension of the Permo-Triassic Siberian Traps, Russia. Lithos, 79: 425-452.

Renne P.R., Black M.T., Zichao Z., Richards M.A. and Basu A.R., 1995. Synchrony and causal relations between Permian-Triassic boundary crises and Siberian flood olcanism. Science, 269: 1413-1416.

Ruban D.A., Al-Husseini M.I. and Iwasaki Y., 2007. Review of Middle East Paleozoic plate tectonics. GeoArabia, 12: 35-55.

Şengör A.M.C., 1990. A new model for the late Palaeozoic-Mesozoic tectonic evolution of Iran and implications for Oman. Geol. Soc. London Spec. Publ., 49: 797-831.

Stampfli G.M., 2000. Tethyan oceans. Geol. Soc. London Spec. Publ., 173: 1-23.

Stampfli G.M., von Raumer J.F. abd Borel G.D., 2002. Paleozoic evolution of pre-Variscan terranes: from Gondwana to the Variscan collision. In: J.R. Martinez Catalan, R.D. Hatcher, R. Arenas and F. Diaz Garcia (Eds.), Variscan-Appalachian dynamics: the building of late Palaeozoic basement. GSA Spec. Paper, 364: 263-280.

Sun S.-S. and McDonough W.F., 1989. Chemical and isotopic systematics of oceanic basalts: implications for mantle composition and processes. Geol. Soc. London Spec. Publ., 42: 313-345.

Tracy R. and Robinson P., 1977. Zoned titanian augite in alkali olivine basalt from Tahiti and the nature of titanium substitutions in augite. Am. Mineral., 62: 634-645.

Vahdati Daneshmand F., 1991. Geological map of Amol, scale 1/250,000. Geol. Survey Iran.

Weaver B.L., 1991. The origin of ocean island basalt end-member compositions: trace element and isotopic constraints. Earth Planet. Sci. Lett., 104: 381-397.

White W.M., 1985. Sources of oceanic basalts: Radiogenic isotopic evidence. Geology, 13: 115-118.

Willbold M. and Stracke A., 2006. Trace element composition of mantle end-members: Implications for recycling of oceanic and upper and lower continental crust. Geochem. Geophys. Geosyst., 7, Q04004, doi: 10.1029/2005GC001005.

Wilmsen M., Fürsich F.T., Seyed-Emami K., Majidifard M.R. and Taheri J., 2009. The Cimmerian Orogeny in northern Iran: tectono-stratigraphic evidence from the foreland. Terra Nova, 21: 211-218.

Wilson M., Guiraud R., Moreau C. and Bellion Y.J.-C., 1998. Late Permian to Recent magmatic activity on the African-Arabian margin of Tethys. Geol. Soc. London Spec. Publ., 132: 231-263.

Winchester J.A. and Floyd P.A., 1977. Geochemical discrimination of different magma series and their differentiation products using immobile elements. Chem. Geol., 20: 325-343.

Xu Y., Chung S.-L., Jahn B.-M. and Wu G., 2001. Petrologic and geochemical constraints on the petrogenesis of Permian-Triassic Emeishan flood basalts in southwestern China. Lithos, 58: 145-168.

Yang S.-F., Li Z., Chen H., Santosh M., Dong C.-W. and Yu X., 2007. Permian bimodal dyke of Tarim Basin, NW China: Geochemical characteristics and tectonic implications. Gondw. Res., 12: 113-120.

Yoder H.S. and Tilley C.E., 1962. Origin of basalt magmas: An experimental study of natural and synthetic rock systems. J. Petrol., 3: 342-532.

Yu X., Yang S.-F., Chen H.-L., Chen Z.-Q., Li Z.-L., Batt G.E. and Li Y.-Q., 2011. Permian flood basalts from the Tarim Basin, Northwest China: SHRIMP zircon U-Pb dating and geochemical characteristics. Gondw. Res., 20: 485-497.

Zanchetta S., Berra F., Zanchi A., Bergomi M., Caridroit M., Nicora A. and Heidarzadeh G., 2013. The record of the Late Palaeozoic active margin of the Palaeotethys in NE Iran: Constraints on the Cimmerian orogeny. Gondw. Res., 24: 1237-1266.

Zanchi A., Zanchetta S., Berra F., Mattei M., Garzanti E., Molyneux S., Nawab A. and Sabouri J., 2009. The Eo-Cimmerian (Late? Triassic) orogeny in north Iran. Geol. Soc. London Spec. Publ., 312: 31-55.

Zhang Y., Liu J. and Guo Z., 2010b. Permian basaltic rocks in the Tarim basin, NW China: Implications for plume-lithosphere interaction. Gondw. Res., 18: 596-610.

Zhang C.-L., Xu Y.-G., Li Z.-X., Wang H.-Y. and Ye H.-M., 2010a. Diverse Permian magmatism in the Tarim Block, NW China: Genetically linked to the Permian Tarim mantle plume? Lithos, 119: 537-552.

Zhou M.-F., Zhao J.-H., Jiang, C.-Y. Gao J.-F., Wang W. and Yang S.-H., 2009. OIB-like, heterogeneous mantle sources of Permian basaltic magmatism in the western Tarim Basin, NW China: Implications for a possible Permian large igneous province. Lithos, 113: 583-594.

Zindler and A. and Hart S., 1986. Chemical geodynamics. Ann. Rev. Earth Planet. Sci., 14: 493-571.

Received, June 23, 2016
Accepted, September 8, 2016